View metadata, citation and similar papers at core.ac.uk

brought to you by CORE

provided by University of Central Florida (UCF): STARS (Showcase of Text, Archives, Research &...

University of Central Florida

STARS

Faculty Bibliography 2010s

Faculty Bibliography

1-1-2010

Cassini Uvis Stellar Occultation Observations of Saturn's Rings

J. E. Colwell
University of Central Florida

L. W. Esposito

R. G. Jerousek
University of Central Florida

M. Sremčević

D. Pettis
University of Central Florida

See next page for additional authors

Find similar works at: https://stars.library.ucf.edu/facultybib2010
University of Central Florida Libraries http://library.ucf.edu

This Article is brought to you for free and open access by the Faculty Bibliography at STARS. It has been accepted for inclusion in Faculty Bibliography 2010s by an authorized administrator of STARS. For more information, please contact STARS@ucf.edu.

Recommended Citation

Colwell, J. E.; Esposito, L. W.; Jerousek, R. G.; Sremčević, M.; Pettis, D.; and Bradley, E. T., "Cassini Uvis Stellar Occultation Observations of Saturn's Rings" (2010). *Faculty Bibliography 2010s*. 61.
https://stars.library.ucf.edu/facultybib2010/61

Authors
J. E. Colwell, L. W. Esposito, R. G. Jerousek, M. Sremčević, D. Pettis, and E. T. Bradley

This article is available at STARS: https://stars.library.ucf.edu/facultybib2010/61

The Astronomical Journal, 140:1569–1578, 2010 December doi:10.1088/0004-6256/140/6/1569
© 2010. The American Astronomical Society. All rights reserved. Printed in the U.S.A.

CASSINI UVIS STELLAR OCCULTATION OBSERVATIONS OF SATURN'S RINGS

J. E. Colwell[1,3], L. W. Esposito[2], R. G. Jerousek[1], M. Sremčević[2], D. Pettis[1], and E. T. Bradley[1]
[1] Department of Physics, University of Central Florida, Orlando, FL 32816-2385, USA; jcolwell@mail.ucf.edu
[2] LASP, University of Colorado, 392 UCB, Boulder, CO 80309-0392, USA
Received 2010 April 28; accepted 2010 September 7; published 2010 October 20

ABSTRACT

The Cassini spacecraft's Ultraviolet Imaging Spectrograph (UVIS) includes a high-speed photometer (HSP) that has observed more than 100 stellar occultations by Saturn's rings. Here, we document a standardized technique applied to the UVIS-HSP ring occultation datasets delivered to the Planetary Data System as higher level data products. These observations provide measurements of ring structure that approaches the scale of the largest common ring particles (∼5 m). The combination of multiple occultations at different viewing geometries enables reconstruction of the three-dimensional structure of the rings. This inversion of the occultation data depends on accurate calibration of the data so that occultations of different stars taken at different times and under different viewing conditions can be combined to retrieve ring structure. We provide examples of the structure of the rings as seen from several occultations at different incidence angles to the rings, illustrating changes in the apparent structure with viewing geometry.

Key words: instrumentation: photometers – methods: observational – planets and satellites: rings – space vehicles: instruments

Online-only material: color figure

1. INTRODUCTION

We present a detailed description of a systematic processing of Cassini Ultraviolet Imaging Spectrograph (UVIS) stellar occultation data. Stellar and radio occultations by Saturn's rings provide the highest resolution profiles of ring structure. The Cassini spacecraft has three instruments that observed high-resolution occultations of the rings: UVIS and the Visual and Infrared Mapping Spectrometer (VIMS) which observe occultations of ultraviolet and infrared stars, respectively, and the Radio Science Subsystem (RSS) which transmits a coherent radio signal through the rings to the Earth. These datasets have revealed evidence for viscous overstability oscillations (Thomson et al. 2007), shown the characteristics of temporary agglomerations of ring particles (Colwell et al. 2006, 2007; Hedman et al. 2007a), revealed small clumps in the F ring (Esposito et al. 2008), and resolved sharp ring edges (Colwell et al. 2008) and short-wavelength waves throughout the rings (Colwell et al. 2009).

Combining multiple occultation profiles from different observing geometries enables reconstruction of the three-dimensional structure of the rings (e.g., Colwell et al. 2006, 2007). This inversion of multiple occultations to obtain information about ring structure is analogous to computed tomography scans in medical imagery with one critical difference: the occultations are widely spaced in time. These data must be appropriately calibrated so that there are no systematic offsets between observations that could be confused with ring structure. In the case of the UVIS High-Speed Photometer (HSP) this involves removal of the background (non-stellar) signal from the data and compensation for a drift in the instrument's sensitivity during the course of an occultation (Colwell et al. 2007).

Cassini observations have revealed the Saturn ring system to be particularly dynamic, with structural changes observed on timescales of years. The structure of the innermost D ring changed significantly between the *Voyager* flybys and the arrival of Cassini (Hedman et al. 2007b). The F ring has undergone fundamental structural changes even during the time Cassini has been in orbit (Albers et al. 2010; Charnoz et al. 2005; Murray et al. 2005), and ephemeral clumps have been observed in the F ring in images (Murray et al. 2008; Beurle et al. 2010) and occultations (Esposito et al. 2008). There are also many clues to the evolution of the remaining main rings (A, B, C, and the Cassini Division) on multiple timescales. The shifting orbits of nearby moons, notably the co-orbital satellites Janus and Epimetheus and the F ring moons Prometheus and Pandora, result in changes to the locations of resonances and the ring structures, primarily density waves, associated with them (e.g., French et al. 2003; Tiscareno et al. 2007). On arrival at Saturn, Cassini discovered evidence of small moonlets, dubbed propeller objects for the characteristic perturbations they produce in the surrounding ring material, in the outer A ring (Tiscareno et al. 2006). The distribution of these moonlets is non-uniform, suggesting a possible origin in the fragmentation of a small number of larger objects (Sremčević et al. 2007; Tiscareno et al. 2008). Serendipitous passes of stellar occultation paths across clumps, moonlets, or their associated disturbances in the nearby ring material, provide high-resolution one-dimensional measurements of structure on the scale of the largest ring particles.

In Section 2, we describe the UVIS stellar occultation data including a tabular summary of all occultations observed to date. In Section 3, we describe a standard procedure for the calibration of the occultation data used to generate the optical depth profiles delivered to the Planetary Data System (PDS). We present examples of these optical depth profiles and discuss the uncertainties in the calibration.

2. OBSERVATIONS

The Cassini UVIS observes stellar occultations by the rings through two channels: the HSP, and the Far Ultraviolet (FUV) spectrograph. The HSP is the primary channel for measuring ring structure because of its fast sampling time of 1–8 ms. The FUV channel is used for simultaneous measurements of the UV ring spectral reflectance as well as for imaging the star and rings to facilitate determination of background levels in the HSP data. The HSP and FUV have the same spectral bandpass

[3] Author to whom any correspondence should be addressed.

of approximately 110–190 nm (Esposito et al. 2004), while the FUV has 1024 spectral resolution elements and 64 spatial resolution elements along the slit. A single FUV integration produces much more data than the HSP which is typically operated in a 9 bit compression mode. The FUV is less sensitive than the HSP and cannot be read out as quickly, so it is not used for measurements of ring structure. However, the imaging capabilities of the FUV do allow simultaneous measurements of the ring brightness in the same part of the spectrum that the HSP measures. Due to data rate limitations, the integration period for these simultaneous FUV observations is typically at least 60 s compared to 1 or 2 ms for the HSP. Although the sensitivities of both the FUV and HSP are changing in different ways as the mission progresses, the total FUV sensitivity to α Vir was $\sim$20,000 counts s^{-1} on the Rev 030 occultation compared to over 500,000 counts s^{-1} observed in the HSP (Table 1). For some occultations, the FUV data can be used in constructing a model of the background component of the HSP signal (Section 3.3; see also Colwell et al. 2007). Because this process depends on additional models of the instrument response and the azimuthal behavior of ring brightness, we do not use the FUV data in determining the background provided to the PDS; instead we provide the FUV data so that interested users can create a new background model making use of this additional information.

The photon count rate, I, measured by the HSP includes light from the star and a background photon count rate, b, and depends on the transparency, T, of the intervening ring material. The background has contributions from interplanetary Lyα emission and sunlight reflected off the rings. The latter component of the background is highly sensitive to the occultation viewing geometry and dominates b for observations of the sunlit face of the rings. The interplanetary Lyα signal is the dominant source of background when the unlit face of the rings is observed. It, too, varies over the course of the occultation due to the different transparency of the rings at different times in the occultation, allowing more or less Lyα to shine through the rings. A direct measurement of b is only possible when there is no signal from the star. This is typically only the case when the star is behind the opaque central B ring, though for fainter stars or occultations at a low elevation angle above the ring plane, B, the star is not detected at other locations. If the measured photon count rate due to the unocculted star alone is I_0, then the measured photon count rate is given by

$$I = I_0 T + b. \tag{1}$$

The count rate due to the unocculted star, I_0, is measured in regions where $T = 1$ and $I = I_0$+b. With the background determined from measurements where $T = 0$ and $I = b$, I_0 can be determined. Tables 2 and 3 list the locations of regions we use to determine b and I_0.

Ignoring stellar variation, I_0 is ideally constant and a single measurement either in a ring gap or outside the rings would be sufficient to determine it for the entire occultation, leaving all the uncertainties in b. While stellar variability is not a significant source of variation or uncertainty in I_0 for any of the UVIS occultations, the HSP does not have a constant response to bright signals. This results in variations in the measured value of I_0 over the course of an occultation so that it can only be precisely determined (ignoring for the moment uncertainties in b) in the sparsely spaced gaps in the rings. The nature of the HSP response to bright signals is shown in Figure 1. When exposed to a bright star, the photon count rate measured by the HSP increases rapidly for several minutes and then increases more

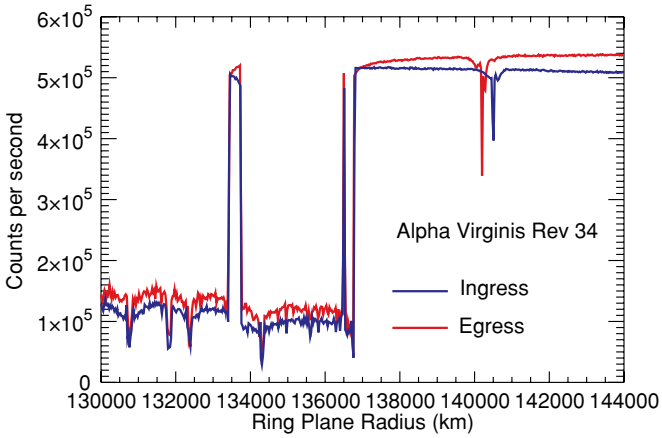

Figure 1. Outer A ring region and the F ring in the ingress (blue) and egress (red) portions of a chord occultation of the star α Virginis. The Encke Gap at 133,500 km illustrates the change in instrument response as a function of its history of exposure. The signal is low when it first crosses the Encke gap edge and gradually increases while it is behind the gap. The instrumental response is also responsible for the offset between the ingress and egress light curves in the region beyond the outer edge of the A ring at 136,750 km. The difference in signal in the A ring is not due to instrumental effects: just inside the gap values of I_0 for both ingress and egress are equal, so the instrument sensitivity is equal at this location for both ingress and egress. Just interior to the inner edge (where I_0 is observed to be the same) values of I are different, and this must therefore not be due to instrumental effects.

gradually. When the star passes behind a gap in the rings, the photon count rate is initially lower than when the star was last previously observed unocculted and then begins to gradually increase again (see also Colwell et al. 2007). The value of I is different when the star is first occulted by a ring and when it emerges from the ring. Without a validated model of the instrument's nonlinear behavior, it is therefore not possible to know what the value of I_0 would be at each point when the star is behind the ring more precisely than the difference in the observed values of I_0 on either side of the ring. The estimated value of the star photon count rate, I_0, is used to calculate the slant path optical depth,

$$\tau = \ln(1/T) = \ln\left(\frac{I_0}{\max[I - b, I_{\min}]}\right), \tag{2}$$

where the denominator is the maximum value of $I - b$ and a selected minimum detectable photon count rate, $I_{\min}$.

Before Equation (2) can be used, the uncertainties in I and b must be estimated, in part to place a lower detectable limit, $I_{\min}$, on the quantity $I - b$. In practice, $I - b$ can be negative due to statistical variations in the data and systematic uncertainties in b. Placing a non-zero minimum value on $I - b$ is equivalent to specifying a maximum normal optical depth that can be distinguished from infinite optical depth, $\tau_{\max}$. In practice, we determine $\tau_{\max}$ based on counting statistics as described in Section 3.3 and calculate the normal (perpendicular to the ring plane) optical depth using $\tau_{\max}$ instead of $I_{\min}$:

$$\tau_n = \min\left[\mu \ln\left(\frac{I_0}{I - b}\right), \tau_{\max}\right], \tag{3}$$

where $\mu = \sin(B)$ with B being the angle between the ring plane and the line of sight from the spacecraft to the star. The normal optical depth at a particular location in the rings varies with the azimuthal viewing geometry due to self-gravity wakes, so that even occultations of the same star yield different optical depth

Table 1
Occultation Summary

Occultation Star (rev) Side	Date (Year–Day)	$\|B\|$ (deg)	ϕ deg)	R (km)	Duration (s)	I_0 (Hz)
ξ2 Cet (A) E	2004–280	14.9	72.9–89.4	57,757–80,239	27197	1,300
ξ2 Cet (A) E	2004–281	14.9	98.8–103.8	108,956–135,650	26199	1,400
126 Tau (8) E	2005–139	21.1	130.2–88.8	70,380–141,390	31888	3,600
α Vir (8) I	2005–141	17.2	116.1–150.2	118,979–141,954	2546	479,000
α Vir (8) E	2005–141	17.2	116.1–82.2	118,979–141,704	2535	509,000
δ Aqr (8) E	2005–141	12.2	106.8–131.4	60,687–169,884	9871	700
α Leo (9) I	2005–159	9.5	68.0–10.7	114,150–204,718	6948	46,500
α Leo (9) E	2005–159	9.5	68.0–98.4	114,150–131,539	2663	43,200
126 Tau (10) I	2005–175	21.1	204.3–216.5	103,210–144,810	15898	4,100
σ Sgr (11) I #	2005–195	29.1	221.9–248.8	85,987–146,929	5721	117,000
α Sco B (13) I	2005–232	32.2	155.0–208.4	101,173–155,751	6873	3600
α Sco B (13) E	2005–232	32.2	155.1–105.8	101,173–146,576	6027	3600
ζ Oph (26) E	2006–206	16.2	126.7–116.6	120,941–149,225	6611	28,000
λ Cet (28) I	2006–256	15.3	304.0–258.5	74,330–144,011	8901	2,500
α Sco B (29) I	2006–269	32.2	327.3–274.2	79,864–149,436	17154	3,500
λ Sco (29) E #	2006–269	41.7	189.1–136.4	88,478–143,801	23518	285,000
α Vir (30) I	2006–285	17.2	266.2–219.8	64,022–151,545	4772	535,000
γ Lup (30) I #	2006–286	47.4	157.1–185.9	83,062–94,587	7467	80,000
γ Lup (30) E #	2006–286	47.4	157.1–102.7	83,062–141,044	18845	80,200
ε Mic (30) E	2006–292	31	189.1–174.6	97,363–140,210	16382	300*
μ PsA (31) I	2006–306	30.4	248.1–284.2	116,605–144,033	20599	800
μ PsA (31) E	2006–306	30.4	248.1–234.8	116,605–119,797	6691	700
γ Peg (32) I	2006–311	20.3	110.7–149.5	103,925–155,444	7712	75,000
γ Lup (32) E #	2006–313	47.4	26.3–38.2	84,310–136,192	7046	74,200
α Ara (32) I	2006–314	54.4	280.9–276.5	61,333–139,786	15231	38,900
μ PsA (32) I	2006–318	30.4	248.1–282.6	118,450–143,457	19683	700
μ PsA (32) E	2006–318	30.4	248.1–245.2	118,450–118,607	1486	500
α Ara (33) I	2006–325	54.4	280.8–276.6	65,886–145,356	15461	38,700
α Vir (34) I	2006–337	17.2	282.1–220.9	74,536–153,654	4061	506,000
α Vir (34) E	2006–337	17.2	282.1–344.6	74,536–160,059	4281	516,000
η Lup (34) I	2006–337	51	325.0–286.1	106,848–135,360	10858	47,600
η Lup (34) E	2006–337	51	325.0–7.9	106,848–143,838	12513	46,300
κ Cen (35) E #	2006–350	48.5	108.9–76.6	68,853–146,169	16765	47,100
α Ara (35) I	2006–351	54.4	221.2–252.0	64,857–130,424	22626	37,900
α Ara (35) E	2006–352	54.4	120.1–113.2	126,867–173,467	13891	37,900
γ Peg (36) I	2006–363	20.3	101.6–156.6	102,296–178,178	9939	73,000
α Peg (36) E	2006–363	20.3	101.6–55.7	102,296–146,785	7172	70,100
δ Per (36) E	2006–364	54	68.3–65.7	66,531–140,886	8312	13,900
κ Cen (36) I #	2007–002	48.5	250.0–237.8	63,531–156,380	18341	44,200
ε Lup (36) E #	2007–003	51	36.7–48.3	63,450–148,837	18431	33,300
α Ara (36) I	2007–005	54.4	3.2–311.6	70,897–113,954	24719	37,500
α Ara (36) E	2007–005	54.4	3.2–55.5	70,897–115,410	25228	35,700
γ Gru (37) I	2007–009	35.1	244.3–265.8	137,190–147,326	11069	7,300
γ Gru (37) E	2007–009	35.1	244.3–219.6	137,190–150,985	12999	6,800
δ Per (37) I	2007–015	54	281.1–258.2	60,054–142,584	11273	13,700
ε Lup (37) I #	2007–020	51	324.8–284.8	99,479–129,588	17628	31,700
ε Lup (37) E #	2007–020	51	324.8–10.9	99,479–142,934	21790	31,500
γ Ara (37) I	2007–022	61	245.6–251.2	121,471–147,952	7591	25,400
γ Ara (37) E	2007–022	61	142.5–117.2	80,500–155,599	22962	27,300
ε PsA (38) I	2007–027	23.7	255.1–299.3	82,195–114,638	8817	2,600
ε PsA (38) E	2007–027	23.7	255.1–239.1	82,195–85,527	2610	2,600
ψ Cen (38) I	2007–038	44.3	260.3–243.8	96,426–150,172	12338	1,100
γ Ara (38) I	2007–041	61	212.6–218.7	87,186–93,028	2860	24,400
ε PsA (39) I	2007–045	23.7	255.0–277.4	86,910–94,013	3534	2,500
ε PsA (39) E	2007–045	23.7	255.0–233.6	86,910–93,340	3357	2,300
δ Per (39) I	2007–049	54	284.1–257.8	55,505–143,284	13131	12,600
χ Cen (39) I	2007–056	47.5	159.9–183.9	98,599–148,429	16186	13,200
θ Ara (40) I	2007–061	53.9	16.3–348.5	130,041–146,853	17211	15,300
θ Ara (40) E	2007–061	53.9	16.3–33.6	130,041–136,092	10120	15,000
γ Gru (40) E	2007–063	61	232.3–181.8	67,340–147,704	14990	7,500
β PsA (40) I	2007–063	29.2	269.5–288.1	119,978–142,564	4846	600
3 Cen (40) E	2007–073	39.3	39.4–37.8	110,987–147,354	7481	5,000
ψ Cen (40) I	2007–073	44.3	216.5–216.9	136,109–149,973	3736	2,500
θ Ara (41) E	2007–078	53.9	63.8–89.4	63,681–152,229	25676	12,100
β Sgr (41) I	2007–079	46.3	38.3–18.2	127,360–135,501	9616	2,700
β Sgr (41) E	2007–079	46.3	38.3–64.6	127,360–141,957	13040	2,900

Table 1
(Continued)

Occultation Star (rev) Side	Date (Year–Day)	$\|B\|$ (deg)	ϕ deg)	R (km)	Duration (s)	I_0 (Hz)
γ Gru (41) I	2007–080	35.1	243.1–294.4	91,528–145,958	13345	8,100
γ Gru (41) E	2007–080	35.1	243.1–193.0	91,528–142,229	12781	7,800
δ Per (41) I	2007–082	54	232.8–240.6	49,260–149,746	10051	12,300
κ Cen (42) I #	2007–092	48.5	141.6–178.0	114,712–142,152	27744	40,900
κ Cen (42) E #	2007–092	48.5	141.6–115.3	114,712–127,824	18632	41,700
β Per (42) I	2007–098	47.4	227.8–230.8	84,461–149,674	5326	19,700
ζ Per (42) I	2007–098	38	328.0–318.1	132,811–134,700	1834	10,100
ζ Per (42) E	2007–098	38	328.0–344.0	132,811–137,957	3046	10,100
μ Sco (43) E #	2007–112	43.4	155.8–162.1	117,000–123,000	4171	76,900
λ Sco (44) I #	2007–129	41.7	211.1–244.4	69,544–141,063	19151	250,000
ζ Ori (47) E #	2007–179	2.66	106.6–99.3	78,770–133,732	3890	180,000
α Sco B (55) E	2008–003	32.2	49.6–68.0	115,023–142,164	7841	2,400
ι Cen (56) E	2008–014	42.7	80.0–77.5	131,856–141,213	2880	853*
ν Cen (57) I (a)	2008–026	48	167.1–174.2	115,269–122,933	3740	38,300
ν Cen (57) I (b)	2008–026	48	142.2–146.3	104,915–105,173	1682	38,300
ν Cen (57) E	2008–026	48	142.2–133.8	104,915–106,010	3479	38,300
SAO205839 (57) I	2008–026	15.3	263.7–262.7	129,999–146,087	3331	11,200
ι Cen (57) E	2008–026	52.5	80.8–76.6	128,120–144,648	5072	945*
κ Cen (57) I #	2008–026	48.5	238.4–239.3	139,320–146,914	1491	20,500
β Lup (57) I	2008–026	49.6	226.2–231.9	119,418–148,147	5906	71,200
δ Lup (57) I	2008–026	47	259.3–260.4	114,919–147,965	5805	48,300
γ Lup (57) I #	2008–026	47.4	261.8–262.3	135,464–148,220	2141	54,200
γ Cnc (58) E	2008–040	21.3	227.9–189.4	77,203–160,536	9156	2,800
β Hya (60) I #	2008–058	38.6	173.7–183.2	121,736–162,267	12341	1000
ζ Cen (60) I	2008–060	53.6	221.1–231.2	66,648–146,507	17320	107,000
δ Per (60) I	2008–062	54	283.9–274.5	54,975–146,216	7570	11,600
ζ Cen (62) E	2008–082	53.6	77.3–67.0	63,689–145,087	17831	107,000
α Ara (63) E	2008–092	54.4	95.8–112.3	73,261–141,566	8531	2,900
α Sex (63) I	2008–095	2.7	271.2–207.7	90,296–202,539	2958	500
α Sex (63) E	2008–095	2.7	271.2–337.4	90,296–223,667	3339	500
δ Cen (64) I #	2008–100	55.6	117.2–127.9	131,696–133,946	5443	63,000
δ Cen (64) E #	2008–100	55.6	117.2–107.9	131,696–133,387	4717	66,000
β Cen (64) E #	2008–101	66.7	137.8–89.7	84,952–151,166	20690	600,000
γ Cas (64) I	2008–102	66.3	177.9–201.9	71,735–119,601	4411	103,000
ε Cen (65) I	2008–110	59.6	221.7–229.0	69,876–148,192	15730	130,000
α Ara (65) E	2008–111	54.4	110.4–112.9	125,009–143,844	2325	25,100
δ Cen (66) I #	2008–119	55.6	117.4–142.4	130,072–143,054	13255	50,500
δ Cen (66) E #	2008–119	55.6	117.4–110.6	130,072–130,974	3416	41,600
δ Cen (68) I #	2008–137	55.6	201.9–203.4	124,551–150,366	4731	46,500
θ Hya (70) I	2008–156	1.4	89.5–17.9	126,499–401,041	3428	3,600
θ Hya (70) E	2008–156	1.4	89.5–160.3	126,499–384,109	3267	2,800
θ Hya (71) I	2008–163	1.4	89.5–23.2	124,439–310,043	2561	4,000
θ Hya (71) E	2008–163	1.4	89.5–153.9	124,439–287,654	2339	3,100
β Cen (75) I #	2008–188	66.7	283.5–264.4	72,427–144,448	9611	592,000
γ Cnc (75) I	2008–190	21.3	79.8–24.1	71,827–130,700	10241	4,400
β Cen (77) I #	2008–202	66.7	282.9–264.4	73,334–144,893	9481	583,000
β Cen (77) E #	2008–203	66.7	34.6–54.4	73,267–143,444	10191	604,000
β Cen (78) E #	2008–210	66.7	23.7–54.8	58,470–145,023	12731	572,000
α Ara (79) I	2008–217	54.4	49.5–354.2	94,195–157,552	10626	24,600
α Ara (79) E	2008–217	54.4	49.5–70.2	94,195–100,266	2874	24,600
β Cen (81) I #	2008–231	66.7	294.4–267.6	72,829–151,692	12191	546,000
β Cen (85) I #	2008–260	66.7	295.3–269.5	73,112–143,414	10991	531,000
α Ara (85) I	2008–261	54.4	49.7–353.3	93,510–160,543	10917	25,100
α Ara (85) E	2008–261	54.4	49.7–106.4	93,510–157,485	10873	24,000
α Ara (86) I	2008–268	54.4	49.7–352.5	93,407–163,471	11220	22,400
α Ara (86) E	2008–268	54.4	49.7–107.2	93,407–160,105	11171	21,400
β Cen (89) I #	2008–290	66.7	296.4–269.8	71,854–141,886	10931	500,000
α Ara (90) I	2008–298	54.4	49.7–352.7	92,106–160,553	10949	20,200
α Ara (90) E	2008–298	54.4	49.7–106.7	92,106–156,650	10812	20,000
α Cru (92) I #	2008–312	68.2	125.0–181.6	77,557–155,730	20861	516,000
β Cen (92) E #	2008–313	66.7	42.7–59.1	50,676–154,574	16180	463,000
θ Hya (94) I	2008–332	1.4	89.5–10.5	83,453–436,956	2994	1800*
θ Hya (94) E	2008–332	1.4	89.5–169.9	83,453–500,646	3446	1800*
β Cen (96) I #	2008–343	66.7	288.6–264.8	72,456–155,341	12582	441,000
α Ara (96) I	2008–344	54.4	46.9–1.6	108,169–150,852	9900	19,800
α Ara (96) E	2008–344	54.4	46.9–94.2	108,169–155,151	10551	19,300

Table 1
(Continued)

Occultation Star (rev) Side	Date (Year–Day)	$\|B\|$ (deg)	ϕ deg)	R (km)	Duration (s)	I_0 (Hz)
δ Cen (98) I #	2008–359	55.6	209.3–212.0	55,447–153,103	14531	36,100
β Cru (98) I	2008–359	65.2	157.3–202.6	58,104–154,683	18080	279,000
α Ara (98) I	2008–360	54.4	42.3–357.4	110,536–154,532	12407	17,200
α Ara (98) E	2008–360	54.4	42.3–86.3	110,536–152,130	12024	17,200
α Cru (100) I #	2009–012	68.2	124.2–164.8	114,050–149,157	14422	438,000
α Cru (100) E #	2009–012	68.2	124.2–83.5	114,050–149,449	14508	418,000
γ Cas (100) E	2009–015	66.3	86.4–66.0	72,440–140,370	9611	56,000
β Cen (102) I #	2009–031	66.7	250.7–248.3	73,243–143,508	10311	369,000
β Cen (104) I #	2009–053	66.7	179.2–220.0	70,203–147,291	27000	365,000
β Cen (104) E #	2009–053	66.7	134.8–94.7	68,934–131,988	15591	365,000
ε Cas (104) I	2009–058	69.9	154.5–198.7	111,694–154,568	15864	4,400
ε Cas (104) E	2009–058	69.9	154.5–111.7	111,694–151,532	15197	4,400
θ Hya (104) I	2009–062	1.4	89.3–3.0	66,876–1051,956	5513	1000*
θ Hya (104) E	2009–062	1.4	89.3–172.5	66,876–561,578	2928	1000*
β Cen (105) I #	2009–065	66.7	199.1–222.0	88,502–158,713	14561	310,000
β Cen (105) E #	2009–065	66.7	121.7–91.5	77,787–147,358	15341	301,000
α Ara (105) I	2009–066	54.4	39.2–343.9	93,917–163,844	19802	15,500
α Ara (105) E	2009–066	54.4	39.2–88.6	93,917–143,382	15969	17,000
ζ Cen (112) I	2009–163	53.6	236.6–241.2	71,486–143,214	16464	53,000
μ Cen (113) I	2009–177	48.7	236.2–240.6	75,975–155,785	16090	9,400
α Lup (113) I	2009–178	53.8	172.4–217.8	83,839–118,956	20269	26,400
α Lup (113) E	2009–178	53.8	172.4–160.9	83,839–85,541	4071	26,400
β Lup (114) I	2009–193	49.6	186.8–217.4	118,474–144,836	16090	24,000*
λ Sco (114) I #	2009–195	41.7	219.6–259.1	110,857–148,227	31840	88,500
σ Sgr (114) I #	2009–198	29.1	332.1–329.2	84,449–149,875	21040	33,300
μ Sgr (115) I	2009–212	24.9	44.1–27.4	90,967–94,935	10104	>200+
μ Sgr (115) E	2009–212	24.9	44.1–80.3	90,967–112,618	24707	>200+
β Per (116) I	2009–223	47.4	153.8–169.6	131,436–135,217	2294	2000*
β Per (116) E	2009–223	47.4	153.8–138.5	131,436–134,741	2206	2200*
α Vir (116) I	2009–223	17.2	245.2–241.9	103,059–144,566	3764	165,000
π4 Ori (117) E	2009–239	3.7	105.2–109.1	68,168–145,300	4811	3300
α Vir (124) E	2010–011	17.2	121.7–124.1	70,494–142,431	6011	165,000
β Lib (124) E	2010–011	15.8	236.9–221.5	115,071–123,509	2756	2900

Notes. Rev refers to the number of the orbit of Cassini around Saturn on which the observation occurred. Cassini revs are numbered 0, A, B, C, 3, 4, and consecutively thereafter. Ranges in ϕ and R are for the entire observation, and the range in ϕ is listed in the order corresponding to the range in R. In some cases, part of the occultation is obscured by the planet. The values listed here are for the full occultation, not just the part where the star is unobstructed. Values of I_0 are approximate mean values. See the text for a discussion of variations in I_0. Durations indicate the time from the start of measurements to the last measurement, including gaps caused by data dropouts. "*" indicates occultations for which the background cannot be directly measured, and the values listed in the I_0 column are I_0+b for those occultations. "+" indicates occultations for which the stellar signal cannot be directly measured, and the values listed in the I_0 column are estimates from other occultations. "#" indicates that there is a detectable signal from more than one star in the data. I and E indicate ingress and egress occultations, respectively.

profiles. This can be seen, for example, in the difference in the photon count rate between the ingress and egress portions of the α Virginis occultation in the A ring (Figure 1). The angle, ϕ, between the radial direction at the point where the line of sight pierces the ring plane and the projection of the occultation line of sight onto the ring plane determines the extent to which light can pass between self-gravity wakes at a given ring radius and elevation angle B (Colwell et al. 2006, 2007; Hedman et al. 2007a; Nicholson & Hedman 2009).

In addition to the variation in sensitivity of the HSP during a single occultation, the average sensitivity of the detector has been declining with use over the course of the mission. The sensitivity has declined linearly with total accumulated counts, with most of the absolute decline occurring during the high-inclination sequence that concluded the Cassini Prime mission and began the Cassini Equinox mission, from early 2008 through early 2009. Thus, absolute counting rates for individual stars and minimum background values have declined over the course of the mission so that each occultation must be individually calibrated. This can be seen in Table 1, for example, by comparing the values of I_0 for β Cen, one of the brightest UV stars we observe, from rev 77 through rev 105 where there is roughly a 50% reduction in sensitivity ("rev" identifies the number of the orbit or revolution of Cassini around Saturn). Table 1 lists the ring stellar occultations observed by UVIS through rev 114. Data were also recorded with the HSP during some VIMS stellar occultations, but in most cases no stellar signal was detected by the HSP from those cool stars so those observations are not included in Table 1.

3. CALIBRATION AND PDS DATA PRODUCT

In order to generate a full profile of τ_n from the data, profiles of b and I_0 are constructed by linearly interpolating between regions where each value can be measured directly, or by extrapolation. The data are recorded as a time series with a constant integration period. One approach for interpolation and extrapolation of b and I_0 would be to work in the original uniformly sampled time domain of the data. The approach we

Table 2
Opaque Regions for Background Determination

Number	Inner Radius (km)	Outer Radius (km)
1	100,190	100,210
2	100,260	100,280
3	100,750	100,770
4	101,780	101,800
5	102,090	102,110
6	103,870	103,890
7	104,460	104,480
8	104,860	104,880
9	105,390	105,410
10	106,100	106,150
11	107,870	107,900

Table 3
Gap Regions for Determination of I_0

Name	Inner Radius (km)	Outer Radius (km)
D Ring	74,420	74,450
G1	75,760	75,800
Colombo	77,770	77,820
Maxwell	87,360	87,400
Dawes	90,213	90,215
Huygens	117,720	117,760
Herschel	118,200	118,210
Herschel	118,270	118,280
Russell	118,605	118,625
Jeffreys	118,935	118,955
Laplace	119,860	119,950
Barnard	120,310	120,312
Encke	133,500	133,700
Keeler	136,495	136,505
Roche	137,000	137,500

Note. Subsets of the gaps were used to avoid eccentric edges and ringlets within the gaps. Full gap boundaries are in Colwell et al. (2009).

adopt is to calculate the location in the ring plane of each data point and then interpolate and extrapolate in the ring plane radius domain. The reason for this choice is that it is variations in the radial structure of the rings that is primarily responsible for variations in b and I_0, rather than temporal variations. The ramp-up instrumental response described in Section 2 and in Colwell et al. (2007) depends both on time and on the history of the signal into the instrument. For ring occultations, this signal is most strongly dependent on structure in the rings. The first step in our data processing is therefore the calculation of the ring intercept point of each sample in the occultation data.

3.1. Calculation of Occultation Geometry

The calculation of occultation geometry is described in detail in French et al. (1993), and we follow that general procedure closely. Here, we summarize the steps we follow to calculate the occultation intercept points. We get the spacecraft trajectory from SPICE kernels at the Navigation and Ancillary Information Facility (NAIF) of the PDS. We use ephemeris kernels with combined spacecraft and planetary state data based on reconstruction of the spacecraft trajectory by the Cassini navigation team. Stellar coordinates, proper motions, and parallax are taken from the *Hipparcos* catalog and are propagated forward from the *Hipparcos* epoch of 1991.25 to the time of the occultation and corrected for parallax to the location of Cassini and for aberration due to motion of Saturn with

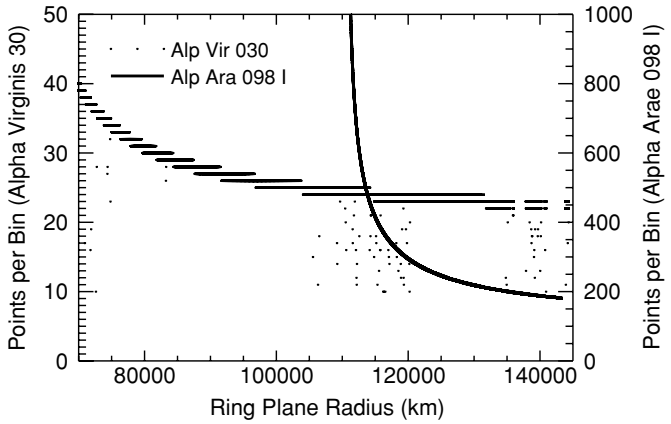

Figure 2. Number of HSP integration periods making up a 1 km radial bin for a radial occultation (α Virginis Rev 30) and a chord occultation (α Arae Rev 98). The minimum radius of the α Arae Rev 98 occultation was 110,536 km, and at that location the number of integrations in a 1 km bin is over 50,000. The scatter in the number of points per bin for the α Vir occultation is due to a large number (104) of data dropouts in that occultation.

respect to the solar system barycenter. The ring plane is assumed to be exactly normal to the pole of Saturn which is retrieved from NAIF planetary constants kernels for the time of the occultation. We make a non-iterative correction for general relativity treating Saturn as a sphere. The general relativistic correction is on the order of 10 m or less. The primary uncertainties are in the position of the spacecraft along its trajectory and the pole direction of Saturn. Based on comparisons of different occultation profiles to features that are circular or nearly so (Nicholson et al. 1990; French et al. 1993), these errors are on the order of 1 km. Ring longitudes are referenced to the ascending node of the ring plane on the J2000 inertial X–Y plane.

3.2. Binning the Data

We next bin the data to a uniform radial scale. The raw data typically have radial sampling intervals of several meters to a few tens of meters, though for occultations that cut a chord across the rings, the radial distance between points essentially vanishes at the minimum ring plane radius sampled by the occultation. To facilitate the intercomparison of occultations and the generation of model profiles of b and I_0, we rebin the data to a radial resolution of 1 km. This process can introduce a small error in the number of counts because we are specifying the new bin boundaries to be separated by exactly 1 km, and the boundaries of the raw data measurements in general do not coincide with the new boundaries. When there are 10 or more raw integration periods within the 1 km bins, we sum the points whose boundaries lie closest to the 1 km bin boundaries. If there are fewer points, we perform a linear interpolation between the two points that straddle the bin boundary and divide the counts in the raw data bin that straddles the boundary of the 1 km bin proportionately between the two adjacent 1 km bins. Figure 2 shows the number of integration periods in 1 km bins for two occultations. The lower-resolution α Virginis rev 030 occultation shows bin-to-bin scatter in the number of integration periods within a bin as well as the effects of numerous data dropouts for this observation (due to poor weather at the Deep Space Network receiving station). The α Arae rev 098 occultation was a grazing, or chord, occultation, so the number of points within a 1 km radial bin is very large at the minimum sampled radius.

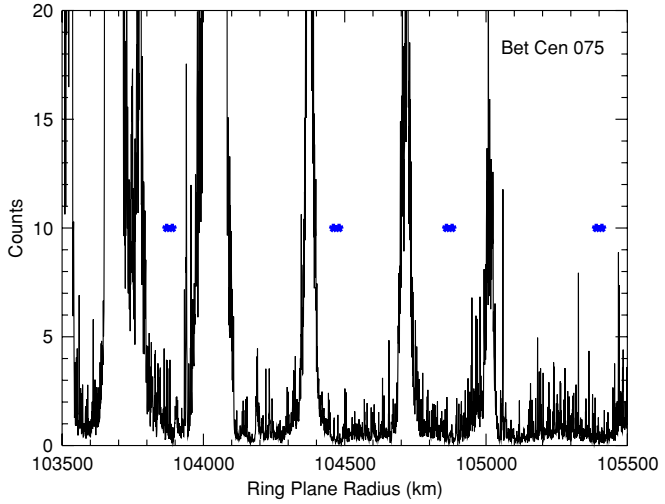

Figure 3. Data from the β Cen Rev 75 occultation showing the central B ring and indicating (asterisks) some of the regions used for determination of the background level (Table 2).

(A color version of this figure is available in the online journal.)

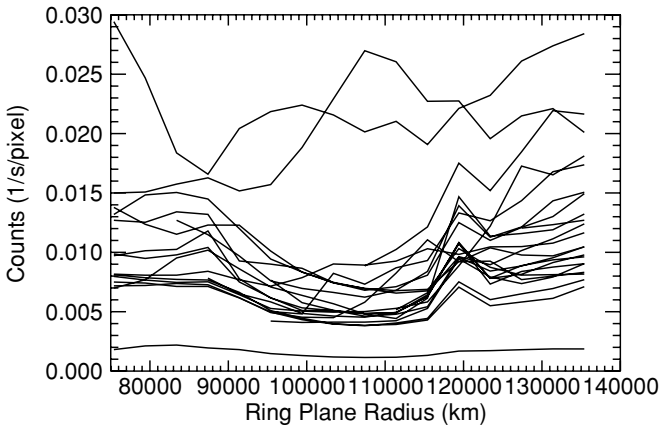

Figure 4. Measured FUV signal for several occultations with the signal from detector rows 28–36 removed. The observations shown are primarily for the unlit face of the rings where Lyα is the dominant source of background, leading to minimum signal in the opaque B ring and larger signals in the more transparent ring regions. Contamination of the signal from the star is also an issue in those regions due to instrument's spatial point spread function.

3.3. Determination of b and I_0

We next identify regions where the star is completely occulted to determine the background photon count rate, b. Parts of the B2 and B3 regions of the B ring have shown no transmitted signal in any occultation (Colwell et al. 2009). The regions we use to determine the background are listed in Table 2. Even in these opaque regions there are hints of structure, but the photon count rates there are reasonable estimates of the background (Figure 3). Determination of b in the C and A ring regions requires either additional data or perfect knowledge of I_0 and τ, so we assume a constant value extrapolated from the B ring region. The Titan ringlet in the inner C ring appears to have narrow opaque regions in the core, interrupted by small-scale ($\sim$1 km) structure, but we do not include this in our standard estimation of b. It is also possible to determine b in regions outside the B ring with simultaneous measurements of the ring UV reflectance with the FUV channel. Colwell et al. (2007) did this for some occultations in their analysis of self-gravity wakes. Their procedure was to measure the FUV signal as a function of ring plane radius and use that as a guide for the radial dependence of the background photon count rate. The background was then normalized by the measured values in opaque regions of the ring. The measured FUV signal on the rings is a combination of scattered sunlight and Lyα transmitted through the rings. FUV data are not available for all occultations, however, and there are complications associated with interpreting FUV data taken during stellar occultations when the star is in the FUV field of view. Some of the star signal gets mislocated onto other rows (see Esposito et al. 1998, 2004 for detailed descriptions of the instrument and its different operational modes). If that signal is attributed to ring or Lyα background, then the background signal would be overestimated.

For those occultations that have coincident FUV data, we derive a radial profile of the FUV signal at 4000 km radial resolution by removing the data that show the signal from the star. This radial profile is obtained from data taken at different longitudes than the HSP occultation data, so the azimuthal asymmetries in ring brightness due to self-gravity wakes (e.g., Franklin and Colombo 1978; Porco et al. 2008) create additional complications in using the FUV data for the background determination. Because of the complications involved in using FUV data for background determination, mentioned above, and because of the partially subjective nature of adapting the FUV profile to the HSP background model, we do not use the FUV data for our standard model of b. Instead we provide the derived FUV radial profile to the PDS for users who wish to use it to develop their own model of b. Examples of the FUV radial profiles are shown in Figure 4.

The image of the star falls near the center of the field of view for the FUV channel (spatial rows 31 and 32, where the rows are numbered 0 to 63 along the UVIS slit). The instrument spatial point spread function causes some of the starlight to bleed over into nearby pixels, so we edit out data in rows 28–36 to remove most of the starlight. The remaining sources of counts in the FUV are Lyα, scattered sunlight, and scattered Saturn-shine. Counts from each of these vary depending on the observational geometry and solar flux levels. For each spatial pixel, we average the raw counts over the spectral pixels in three wavelength ranges from 1118–1911 Å (the full extent of the spectrum), 1700–1911 Å (the long-wavelength portion of the spectrum), and 1199–1224 Å (Lyα). We use raw counts because the sensitivity of the FUV detector with wavelength is close to that of the HSP. Thus, the raw signals recorded by both the FUV and the HSP are roughly proportional to each other. We divide the rings into 4000 km radial bins from the inner C ring to the outer A ring. We then determine the projected field of view of each spatial pixel on the ring plane for each of the four corners of the pixel at the initial and final times for an integration period and determine a minimum and maximum ring plane radius for that pixel over the course of the integration period. For each radial bin, we average the spectral averages for all pixels where their minimum and maximum radial extent falls within the bin, resulting in three count levels for each radial bin, one for each of the three wavelength ranges.

The minimum background in the HSP has been established by a number of observations of the shadowed rings and dark sky (Chambers et al. 2008) as well as observations of VIMS stellar occultations. The HSP count rates in these observations were typically between 100 and 150 counts s^{-1} in measurements made in 2004–2005. The signal observed from stars ranges from a few thousand counts per second to several hundred thousand counts per second. In some cases, the scattered sunlight

background signal can be up to ~10 times higher than the dark sky count rate and can be a significant fraction of the overall signal for faint stars. Although it is not a practical concern because we analyze each occultation independently, it is important to remember that the overall HSP sensitivity is declining with total accumulated exposure such that the background levels observed later in the mission are at lower absolute counting rates than those reported in Chambers et al. (2008) and Colwell et al. (2007).

Our standard procedure for estimating b outlined here, based only on opaque regions in the central B ring, likely underestimates b elsewhere in the rings because we simply assume a constant value of b from the B ring regions to the edges of the ring system. FUV data, where available, and the signal in apparently opaque regions of the Titan ringlet suggest that the background may roughly double from the central B ring to the inner C ring and to the outer A ring (Figure 4). For many occultations the background signal is negligible, and the derived optical depths are insensitive to systematic uncertainties in the background. Drifts in the instrument's sensitivity within an occultation make it difficult to identify broad, low-optical-depth features within gaps and also complicate the determination of the appropriate value of the star brightness to use.

The unobstructed stellar photon count rate, I_0, is modeled by taking measurements in transparent regions in the rings where the observed photon count rate is I_0+b and subtracting the modeled background photon count rate. We use linear interpolation between the gaps in the rings and assume a constant value of I_0 beyond the innermost and outermost gaps. Within some of the broader gaps, notably the Huygens Gap and the Encke Gap, the observed photon count rate changes noticeably due to the changing detector response (e.g., Figure 1). We do not model this changing signal within a gap; we use the simpler technique of taking an average gap value and doing linear interpolation between gaps so that the instrumental effect is clear and we do not risk convolving the effects of broad faint rings, known to exist in some gaps, with our modeling of I_0. We use gaps in the A ring, C ring, and Cassini Division, as well as the Roche Division between the A and F rings, and the optically thin outer D ring (exterior to the D73 ringlet) to determine I_0 (Table 3). When the nominal geometric solution of an occultation leads to a misalignment of the gap with our nominal ranges, we manually adjust the fit to use only data actually within the gap.

3.4. Estimated Maximum Detectable Optical Depth

With the data binned to a common 1 km radial grid and with a model of both I_0 and b, we use Equation (3) to generate a normal optical depth profile. We select $\tau_{\rm max}$ to be the largest normal optical depth that has a finite 1σ upper error bar. The upper error bar in the measured normal optical depth, $\tau_{\rm n}$, based only on counting statistics (and not on systematic uncertainties in modeling I_0 and b as described above) is given by (Colwell et al. 1990)

$$\tau_+ = \mu \ln I_0 - \mu \ln[I_0 e^{-\tau_n/\mu} - Z\sqrt{I_0 e^{-\tau_n/\mu} + b}], \qquad (4)$$

where the quantity under the radical is simply the measured photon count rate I, Z is the number of standard deviations for the error bar, and we use $Z = 1$. Our criterion for $\tau_{\rm max}$ is thus obtained from requiring the term in square brackets in Equation (4) to be positive, or

$$\tau_{\rm max} = \mu \ln[I_0/\sqrt{I}]. \qquad (5)$$

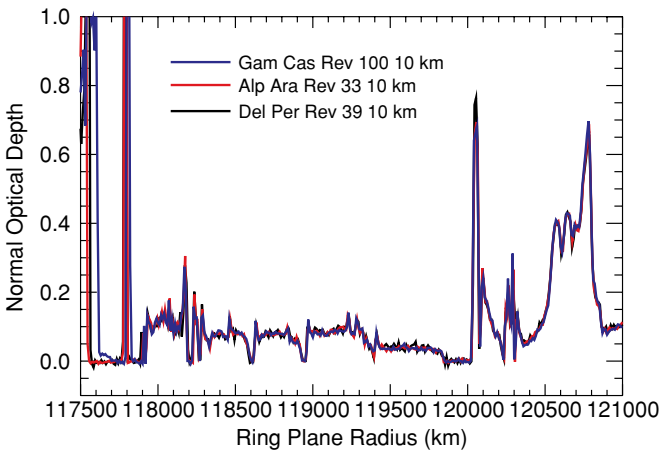

Figure 5. Three optical depth profiles of the Cassini Division at 10 km resolution. The optical depth in the Huygens Gap is not uniformly zero in the γ Cas Rev 100 occultation profile due to the instrumental effects described in the text. Each of these three stars is far above the ring plane ($B > 54°$, Table 1), so the effects of self-gravity wakes on the measured optical depth are not noticeable.

Because the measured photon count rate, I, can be zero, we also require the denominator in Equation (5) to be at least 1, representing one photon count in the bin. As the spatial resolution is degraded by increasing the number of points, n, in a bin, the value of $\tau_{\rm max}$ increases roughly as $\ln\sqrt{n}$. The fractional increase in $\tau_{\rm max}$ as the resolution is decreased depends on the numerical values of I, I_0, and n. Furthermore, in order to assign a complete confidence level to any particular measurement of $\tau_{\rm n}$, systematic uncertainties in both b and I_0 must be estimated and combined with the statistical uncertainty introduced by low counting rates in high optical depth regions (see the discussion in Colwell et al. 2007).

Uncertainties in the calculated optical depths are smallest on an absolute basis at low optical depths, but are smallest in relative terms at intermediate values of the optical depth, with the precise value depending on the brightness of the star. The relative error in $\tau_{\rm n}$ has a broad minimum, is proportional to $\sqrt{I_0}$ for $\tau_{\rm n}$ not close to $\tau_{\rm max}$, and is less than a few percent for $\tau_{\rm n}$ between 0.1 and $\sim\tau_{\rm max}/2$ if $I_0 > 10^5$. The minimum relative error is at a line-of-sight optical depth of $\tau = 2$.

3.5. Calibrated PDS Optical Depth Profiles

The calibrated data are delivered to the PDS at 1 km and 10 km resolutions on identical radial grids so that occultations can be directly compared to each other. The delivered data products include $\tau_{\rm max}$ and $\tau_{\rm n}$ so that whenever $\tau_{\rm n} = \tau_{\rm max}$ in the data, the user knows that this is essentially a lower limit on $\tau_{\rm n}$. In addition to the optical depth, the data files include the ring plane radius, inertial ring longitude, and ephemeris time (relative to J2000) at the center of the bin. The number of raw data points included in the bin (n) and the value of the raw data are also included, as is the model value for I_0 and b. This provides enough information for a user to use the calibration model to resample the data to arbitrary resolution, including full resolution, and to experiment with modified models for I_0 and b. The dataset ID in the PDS is CO-SR-UVIS-2/4-OCC-V1.0.

Examples of radial optical depth profiles calculated following the procedure described above at 1 km and 10 km radial resolution are shown in Figures 5–9. The central part of the B ring contains regions which remain opaque to our brightest,

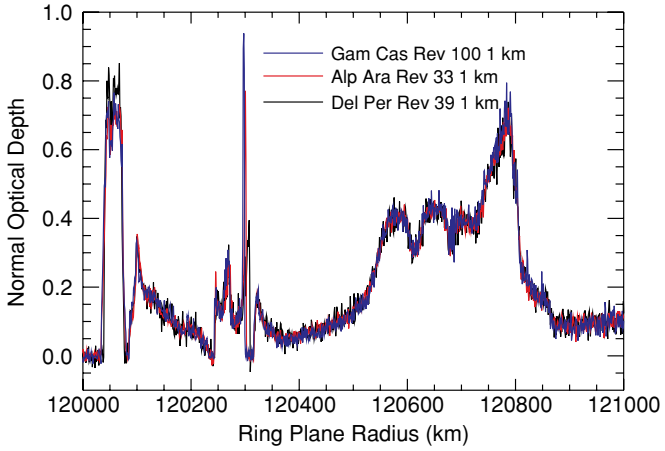

Figure 6. Three optical depth profiles of the outer Cassini Division at 1 km resolution from the same occultation profiles as shown in Figure 5.

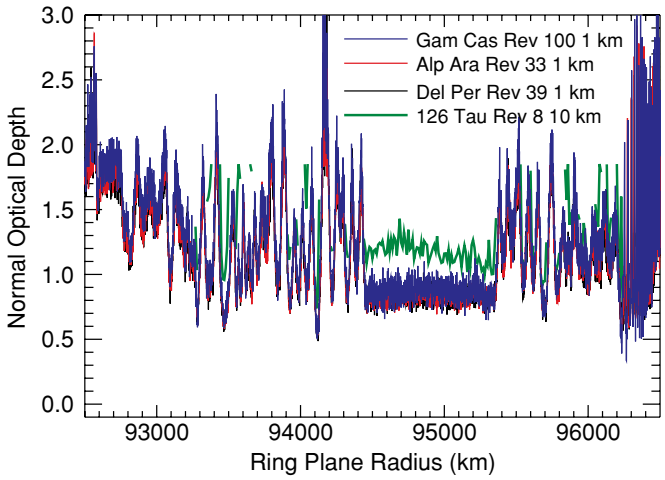

Figure 7. Comparison of optical depth profiles in the inner B ring at 1 and 10 km from four different occultations. The star 126 Tauri has $B = 21.^{\circ}1$, so the presence of self-gravity wakes affects the measured optical depth resulting in a noticeable difference between the profile for that star and the other three that are closer to normal incidence (Colwell et al. 2007).

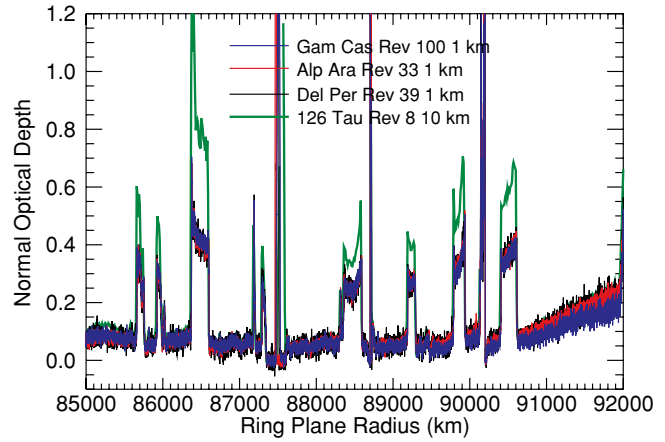

Figure 8. Four optical depth profiles of the outer C ring using the same occultations as shown in Figure 5. The 126 Tauri is shown at 10 km resolution because the star is fainter than the other three. There is a smaller offset in the low-τ regions that may indicate that the background for the 126 Tauri is overestimated (see also Colwell et al. 2007 for a detailed discussion of this occultation and its complicated background).

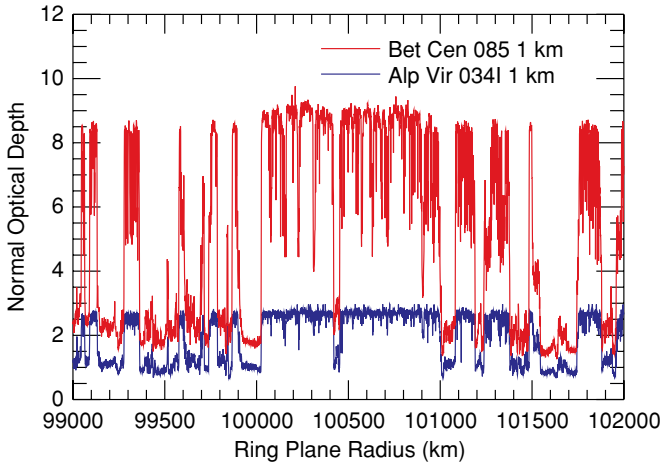

Figure 9. Optically thick region of the B ring seen in two occultations at very different incidence angles. The high incidence angle β Centauri occultation is able to measure much larger normal optical depths, and this region of the rings remains opaque at this geometry: $\tau = \tau_{\rm max}$ for both stars over much of this and other regions in the B ring. Where τ is measured, it differs between the two stars due to the effect of self-gravity wakes (Colwell et al. 2007). Some high optical depth structure that is only suggested by the α Virginis occultation shows up at $\tau \sim 5$ in the β Centauri occultation.

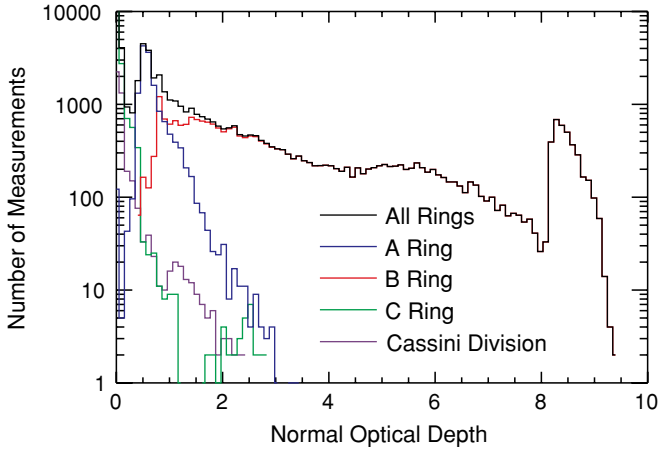

Figure 10. Histograms of optical depth measurements from the β Centauri (Rev 085; see Figure 9) occultation. The peak at large optical depth reflects $\tau_{\rm max}$. A smaller, broader peak at τ = 5–6 reflects real measurements of transmitted starlight in the central B ring.

highest-incidence angle stars (Figure 9). Figure 10 shows the distribution of measured normal optical depths from an occultation of β Centauri ($B = 66.^{\circ}7$). There is a shallow distribution of $\tau_{\rm n}$ in the B ring and a significant number of measurements where $\tau_{\rm n} = \tau_{\rm max}$ (5.3% of the total number of ring measurements and 13% of all measurements in the B ring at 1 km resolution). Only the B ring has these opaque regions in the brightest star occultations observed by UVIS.

4. SUMMARY

The Cassini UVIS has observed over 100 stellar occultations by Saturn's rings with its HSP through the first 6 years of its orbital tour of the Saturn system. These occultations span a variety of viewing geometries and star brightnesses (Table 1). Occultations at different viewing geometries can reveal vertical and non-axisymmetric structure in the rings. Even occultations of bright stars at high incidence angle reveal significant regions in the B ring that are opaque, with a nominal minimum optical depth ~10 at 1 km resolution.

Comparison of the optical depth of the rings (or equivalently the transparency) between occultations in order to extract information about this structure requires careful consideration of instrumental effects and background signal, as well as a resampling of the data to a common radial sampling grid. We describe here a standard procedure for producing optical depth profiles from the UVIS HSP star occultations. These profiles are delivered to the PDS as they are generated. Researchers can resample the data to any desired resolution using the data products provided which include models of the background and star intensity, as well as supplementary data on the ring reflectivity for use in deriving more refined background models.

This work was supported by NASA through the Cassini project and by the Cassini Data Analysis Program, grants NNX08AQ73G and NNX10AF20G. We appreciate the detailed review of an anonymous referee whose comments improved the paper. We thank the entire Cassini Rings Target Working Team and in particular Jeff Cuzzi, Phil Nicholson, Kelly Perry, and Brad Wallis whose efforts made these observations possible.

REFERENCES

Albers, N., Sremčević, M., Colwell, J. E., & Esposito, L. W. 2010, Icarus, submitted
Beurle, K., Murray, C. D., Williams, G. A., Evans, M. W., Cooper, N. J., & Agnor, C. B. 2010, ApJ, 718, L176
Chambers, L. S., Cuzzi, J. N., Asphaug, E., Colwell, J. E., & Sugita, S. 2008, Icarus, 194, 623
Charnoz, S., Porco, C. C., Déau, E., Brahic, A., Spitale, J. N., Bacques, G., & Baillié, K. 2005, Science, 310, 1300
Colwell, J. E., Esposito, L. W., & Sremčević, M. 2006, Geophys. Res. Lett., 33, L07201
Colwell, J. E., Esposito, L. W., Sremčević, M., Stewart, G. R., & McClintock, W. E. 2007, Icarus, 190, 127
Colwell, J. E., Jerousek, R. G., & Esposito, L. W. 2008, BAAS, 40, 443
Colwell, J. E., Nicholson, P. D., Tiscareno, M. S., Murray, C. D., French, R. G., & Marouf, E. A. 2009, in Saturn from Cassini-Huygens, ed. M. K. Dougherty, L. W. Esposito, & S. M. Krimigis (Dordrecht: Springer), 375
Colwell, J. E., et al. 1990, Icarus, 83, 102
Esposito, L. W., Colwell, J. E., & McClintock, W. E. 1998, Planet. Space Sci., 46, 1221
Esposito, L. W., Meinke, B. K., Colwell, J. E., Nicholson, P. D., & Hedman, M. M. 2008, Icarus, 194, 278
Esposito, L. W., et al. 2004, Space Sci. Rev., 115, 299
Franklin, F. A., & Colombo, G. 1978, Icarus, 33, 279
French, R. G., McGhee, C. A., Dones, L., & Lissauer, J. J. 2003, Icarus, 162, 143
French, R. G., et al. 1993, Icarus, 103, 163
Hedman, M. M., Nicholson, P. D., Salo, H., Wallis, B. D., Buratti, B. J., Baines, K. H., Brown, R. H., & Clark, R. N. 2007a, AJ, 133, 2624
Hedman, M. M., et al. 2007b, Icarus, 188, 89
Murray, C. D., Beurle, K., Cooper, N. J., Evans, M. W., Williams, G., & Charnoz, S. 2008, Nature, 453, 739
Murray, C. D., Chavez, C., Beurle, K., Cooper, N., Evans, M. W., Burns, J. A., & Porco, C. C. 2005, Nature, 437, 1326
Nicholson, P. D., Cooke, M. L., & Pelton, E. 1990, AJ, 100, 1339
Porco, C. C., Weiss, J. W., Richardson, D. C., Dones, L., Quinn, T., & Throop, H. 2008, AJ, 136, 2172
Sremčević, M., Schmidt, J., Salo, H., Seiss, M., Spahn, F., & Albers, N. 2007, Nature, 449, 1019
Thomson, F. S., Marouf, E. A., Tyler, G. L., French, R. G., & Rappaport, N. J. 2007, Geophys. Res. Lett., 34, L24203
Tiscareno, M. S., Burns, J. A., Hedman, M. M., & Porco, C. C. 2008, AJ, 135, 1083
Tiscareno, M. S., Burns, J. A., Hedman, M. M., Porco, C. C., Weiss, J. W., Dones, L., Richardson, D. C., & Murray, C. D. 2006, Nature, 440, 648
Tiscareno, M. S., Burns, J. A., Nicholson, P. D., Hedman, M. M., & Porco, C. C. 2007, Icarus, 189, 14